UNIVERSITY
OF TRENTO

DEPARTMENT OF INFORMATION AND COMMUNICATION TECHNOLOGY

38050 Povo – Trento (Italy), Via Sommarive 14
http://www.dit.unitn.it

DETECTION, LOCATION AND IMAGING OF MULTIPLE SCATTERERS BY MEANS OF THE ITERATIVE MULTISCALING METHOD

Salvatore Caorsi, Andrea Massa and Massimo Donelli

July 2003

Technical Report # DIT-03-044

Also: submitted for consideration for publication 'IEEE Transactions on Microwave Theory and Techniques'

Detection, Location and Imaging of Multiple Scatterers by means of the Iterative Multiscaling Method

Salvatore Caorsi*, Massimo Donelli**, and Andrea Massa**

*Department of Electronics

University of Pavia, Via Ferrata 1, 27100 Pavia - Italy

Tel. +39 0382 505661, Fax +39 0382 422583

**Department of Information and Communication Technology

University of Trento, Via Sommarive 14, 38050 Trento - Italy

Tel. +39 0461 882057, Fax +39 0461 882093, E-mail: *andrea.massa@ing.unitn.it, massimo.donelli@dit.unitn.it*

Detection, Location and Imaging of Multiple Scatterers by means of the Iterative Multiscaling Method

Salvatore Caorsi*, Massimo Donelli**, and Andrea Massa**

Abstract

In this paper, a new version of the iterative multiscaling method (IMM) is proposed for reconstructing multiple scatterers in two-dimensional microwave imaging problems. The manuscript describes the new procedure evaluating the effectiveness of the IMM previously assessed for single object detection. Starting from inverse scattering integral equations, the problem is recast in a minimization one by defining iteratively (at each level of the scaling procedure) a suitable cost function allowing firstly a detection of the unknown objects, successively a location of the scatterers and finally a quantitative reconstruction of the scenario under test. Thanks to its properties, the approach allows an effective use of the information achievable from inverse scattering data. Moreover, the adopted kind of expansion is able to deal with all possible multiresolution combinations in an easy and computationally inexpensive way. Selected numerical examples concerning dielectric as well as dissipative objects in noisy environments or starting from experimentally-acquired data are reported in order to confirm the usefulness of the introduced tool and of the effectiveness of the proposed procedure.

Key words:

Microwave Imaging, Inverse Scattering, Iterative Multiscaling Method, Multiple Scatterers Retrieval.

1 Introduction

Microwave imaging techniques based on the solution of an inverse scattering problem are aimed at retrieving an unknown dielectric profile starting from the knowledge of scattered fields radiated by the unknown scenario after the illumination with known incident electromagnetic waves. Unfortunately, the information content of the data is limited and consequently the resolution accuracy in the retrieval of the dielectric profile [1]. In many applications (e.g., demining applications or non-invasive archeological surveys [2], or non-destructive industrial evaluations [3] and testing [4]), a simple qualitative reconstruction is not sufficient and a more difficult qualitative retrieval with an higher resolution level is necessary. In order to fully exploit the information content of the data and to achieve a sufficient resolution accuracy, multiresolution approaches have been proposed [5]-[10]. The guidelines of these approaches lie in the following idea. It is not necessary to attain the same resolution level in the overall scenario under test, but different regions of the investigation domain require different resolution accuracies depending on the homogeneity of the area.

In this framework, the Iterative Multiscaling Method (IMM) is based on a synthetic zoom procedure allowing an efficient use of the limited amount of the information content of inverse scattering data and guaranteeing a sufficient resolution level in the retrieved image of the investigation domain. Starting from a coarse representation of the investigation domain, the method iteratively defines a sub-gridding of the area where the scatterers are located. The approach estimates the scatterers location and occupation area thanks to the "knowledge" of the scenario under test acquired at the previous steps and terminates when a "stationary" reconstruction is reached. In [9][10], the method has been successfully applied to the localization, shaping and dielectric permittivity reconstruction of single inhomogeneous two-dimensional scatterers. In this paper, the IMM is applied to the reconstruction of multiple objects, in order to assess its effectiveness in resolving different scatterers.

The manuscript is organized as follows. In Section II, the mathematical formulation of the IMM is described and detailed for the electromagnetic imaging of multiple scatterers. Numerical experiments, validating the proposed approach, are presented in Section III. Finally, (Section IV) brief conclusions follow.

2 Mathematical Formulation

To illustrate the inversion procedure, the theoretical model of the two-dimensional inverse scattering problem is considered. A bounded investigation domain, D_I, embedding an unknown non-magnetic scattering object, lies in an unbounded homogeneous background medium of known dielectric characteristics, τ_0 (Fig. 1). In order to reconstruct the contrast function of the unknown object, $\tau(x,y) = \varepsilon_r(x,y) - 1 - j\frac{\sigma(x,y)}{2\pi f \varepsilon_0}$, $(x,y) \in D_O \subset D_I$, the investigation domain is successively illuminated by a number of V incident monochromatic (f being the working frequency) electromagnetic fields, $E^v_{inc}(x,y)$, $v = 1,...,V$. The scattered data, $E^v_{scatt}\left(x_{m_{(v)}}, y_{m_{(v)}}\right)$, $m_{(v)} = 1, \ldots, M_{(v)}$, $v = 1,...,V$, are measured by receiver arrays positioned in $M_{(v)}$ positions of an observation domain, D_M, outside the investigation domain. The electromagnetic model linking the available data and the structure of τ is mathematically described by means of the Lippmann-Schwinger integral equations [11]:

$$E^v_{scatt}(x_{m(v)}, y_{m(v)}) = k_0^2 \int_{D_I} G_{2d}(x_{m(v)}, y_{m(v)}|x', y')\tau(x', y')E^v_{tot}(x', y')dx'dy', \quad m_{(v)} = 1, ..., M_{(v)} \quad v = 1, ..., V \tag{1}$$

$$E^v_{inc}(x,y) = E^v_{tot}(x,y) - k_0^2 \int_{D_I} G_{2d}(x,y|x',y')\tau(x',y')E^v_{tot}(x',y')dx'dy' \quad v = 1,...,V \tag{2}$$

where G_{2d} denotes the Green function of the background medium [12]. Due to the nonlinear nature of the problem at hand, nonlinear inversion procedures recast the solution

of Eqs. (1)-(2) as the minimization of a cost functional, enforcing fidelity to the data, defined as follows

$$\Phi\left\{\tau(x,y),\,(x,y)\in D_O;\,E^v_{tot}(x,y),\,(x,y)\in D_I\right\}= \\ \frac{\sum_{v=1}^{V}\left|E^v_{inc}(x,y)-\left[E^v_{tot}(x,y)-k_0^2\int_{D_I}G_{2d}(x,y|x',y')\tau(x',y')E^v_{tot}(x',y')dx'dy'\right]\right|^2}{\sum_{v=1}^{V}\left|E^v_{inc}(x,y)\right|^2}+ \\ \frac{\sum_{v=1}^{V}\sum_{m(v)=1}^{M(v)}\left|E^v_{scatt}(x_{m(v)},y_{m(v)})-\left[k_0^2\int_{D_I}G_{2d}(x_{m(v)},y_{m(v)}|x',y')\tau(x',y')E^v_{tot}(x',y')dx'dy'\right]\right|^2}{\sum_{v=1}^{V}\sum_{m(v)=1}^{M(v)}\left|E^v_{scatt}(x_{m(v)},y_{m(v)})\right|^2} \tag{3}$$

by assuming a proper representation of the unknown functions. Due to the limited amount of the information content of the data, the choice of an uniform discretization of the unknowns on the overall investigation domain strongly limits the resolution-accuracy of the reconstruction procedure. In order to reduce the overall blurring effects on the recovered profile and significantly improving the imaging quality, rather than parameterizing the problem in term of a large number of pixel values, a number of unknowns equal to essential dimension of the space of the data is looked for. Moreover, in order to guarantee the required spatial resolution in different regions of the investigation domain, the object function is represented by means of a multiresolution expansion distributing in a nonuniform way the problem unknowns. However, if an *a-priori* estimate of the distribution of the unknowns in the investigation domain needs of *a-priori information* of the scenario under test (in principle, not always available), an iterative re-allocation of the unknowns by means of an *adaptive multi-resolution* procedure guarantees a blind reconstruction procedure allowing to insert into the reconstruction process the "acquired" information (at the previous steps) about the scenario under test. Such an approach has been proposed in [10] in order to image single scatterers by defining the multi-resolution cost function whose expression at s-th step results

$$\Phi^{(s)}\left\{\tau\left(x_{n_{(r)}},y_{n_{(r)}}\right),\ E^v_{tot}\left(x_{n_{(r)}},y_{n_{(r)}}\right);\ r=1,...,R=s;\ n_{(r)}=1,...,N_{(r)};\ v=1,...,V\right\}=$$
$$\left\{\sum_{v=1}^{V}\sum_{m_{(v)}=1}^{M_{(v)}}\left|E^v_{scatt}\left(x_{m_{(v)}},y_{m_{(v)}}\right)-\sum_{r=1}^{R}\sum_{n_{(r)}=1}^{N_{(r)}}\left\{w\left(x_{n_{(r)}},y_{n_{(r)}}\right)\tau\left(x_{n_{(r)}},y_{n_{(r)}}\right)\right.\right.$$
$$\left.E^v_{tot}\left(x_{n_{(r)}},y_{n_{(r)}}\right)G_{2d}\left(A_{n_{(r)}},\rho_{n_{(r)}m_{(v)}}\right)\right\}\Big|^2\Big\}+\left\{\sum_{v=1}^{V}\sum_{r=1}^{R}\sum_{n_{(r)}=1}^{N_{(r)}}\right.$$
$$\left\{w\left(x_{n_{(r)}},y_{n_{(r)}}\right)\left|E^v_{inc}\left(x_{n_{(r)}},y_{n_{(r)}}\right)-\left[E^v_{tot}\left(x_{n_{(r)}},y_{n_{(r)}}\right)\right.\right.$$
$$\left.\left.\left.+\sum_{q_{(r)}=1}^{N_{(r)}}\left\{\tau\left(x_{q_{(r)}},y_{q_{(r)}}\right)\ \ E^v_{tot}\left(x_{q_{(r)}},y_{q_{(r)}}\right)G_{2d}\left(A_{q_{(r)}},\rho_{q_{(r)}n_{(r)}}\right)\right\}\right]\right|\Big\}^2\Big\} \tag{4}$$

where, w, is a weighting function

$$w(x_{n_{(r)}},y_{n_{(r)}})=\begin{cases}0\ if\ (x_{n_{(r)}},y_{n_{(r)}})\notin D_{(s-1)}\\ 1\ if\ (x_{n_{(r)}},y_{n_{(r)}})\in D_{(s-1)}\end{cases}$$

, $A_{n_{(r)}}$is the area of the n-th discretization domain at the r-th resolution level, and $\rho_{n_{(r)}m_{(v)}}=\sqrt{\left(x_{n_{(r)}}-x_{m_{(v)}}\right)^2+\left(y_{n_{(r)}}-y_{m_{(v)}}\right)^2}$, $\rho_{q_{(r)}n_{(r)}}=\sqrt{\left(x_{q_{(r)}}-x_{n_{(r)}}\right)^2+\left(y_{q_{(r)}}-y_{n_{(r)}}\right)^2}$. In order to take into account for the presence of multiple scatterers the IMM needs of the following procedural operations iteratively repeated at each step, s, of the multi-scaling approach:

- a *Clustering Procedure* aimed at defining the number, Q, of scatterers in the investigation domain and the regions, $D_O^{(q)}$, $q=1,...,Q$, where the synthetic zoom will be performed;
- a *Retrieval Procedure* aimed at reconstructing the dielectric profile in each region, $D_O^{(q)}$, defined by the *clustering procedure*;
- a *Termination Procedure* aimed at stopping the multi-step procedure when a "stationary" reconstruction is achieved.

2.1 Clustering Procedure

Let us assume that the grey-level representation of reconstructed dielectric profile of the scenario under test at s-th step be as in Fig. $2(a)$. Firstly, the pixel representation of

the estimated profile is binarized by *thresholding*. More in detail, the histogram of the image (Fig. $2(b)$) is examined and an histogram-concavity analysis is employed in order to define a threshold value, T_τ. Then, the original image is segmented into two regions (Fig. $2(c)$), namely the object and the background region, as follows

$$\tau_{th}(x_{n_{(r)}}, y_{n_{(r)}}) = \begin{cases} \tau_0 & if\ \tau(x_{n_{(r)}}, y_{n_{(r)}}) < T_\tau \\ \tau_{max} & elsewhere \end{cases} \tag{5}$$

being τ_{max} the maximum value of the object function in the investigation domain at the s-th step.

Successively, a noise filtering (Fig. $2(d)$) is performed in order to eliminate some artifacts and clearly defining the scatterers support by means of the following transformation

$$\tau_{dn}(x_{n_{(r)}}, y_{n_{(r)}}) = \begin{cases} \tau_0 & if \quad \tau_{th}(x_j, y_j) = \tau_0,\ j = 1, ., N_p \\ \tau_{max} & if \quad \tau_{th}(x_j, y_j) = \tau_{max},\ j = 1, ., N_p \\ \tau_{th}(x_{n_{(r)}}, y_{n_{(r)}}) & elsewhere \end{cases} \tag{6}$$

where (x_j, y_j) indicates a neighboring position and N_p is the dimension of the complete neighborhood system of the sub-domain located at $(x_{n_{(r)}}, y_{n_{(r)}})$.

Finally, the *object-detection* is performed. The binarized image is raster scanned left to right and top to bottom. The current pixel, $(x_{n_{(r)}}, y_{n_{(r)}})$ (Fig. $2(e)$), is labeled as belonging to an object or to the background by examining its connectivity to the right-hand neighbors, $(\widehat{x}_j, \widehat{y}_j)$, $j = 1, ., N_p^{(rh)}$. For example, if $\tau_{dn}(x_{n_{(r)}}, y_{n_{(r)}}) = \tau_{max}$, then it is assigned to the object q to which it is connected. A new object-label $(q+1)$ is assigned when a transition from a background-pixel to an isolated object-pixel is detected. At the end of the scan, features such as centroid

$$x^{(q)}_{c_{(s-1)}} = \frac{x^{(q)}_{re_{(s-1)}} + x^{(q)}_{im_{(s-1)}}}{2}, \quad y^{(q)}_{c_{(s-1)}} = \frac{y^{(q)}_{re_{(s-1)}} + y^{(q)}_{im_{(s-1)}}}{2} \tag{7}$$

being

$$x^{(q)}\left\{\begin{array}{c} re \\ im \end{array}\right\}_{(s-1)} = \frac{\sum_{r=1}^{R}\sum_{n_{(r)}=1}^{N_{(r)}}\left\{x_{n_{(r)}}^{(q)}\left\{\begin{array}{c} Re \\ Im \end{array}\right\}\left[\tau_{dn}^{(q)}\left(x_{n_{(r)}},y_{n_{(r)}}\right)\right]\right\}}{\sum_{n_{(r)}=1}^{N_{(r)}}\left\{\left\{\begin{array}{c} Re \\ Im \end{array}\right\}\left[\tau_{dn}^{(q)}\left(x_{n_{(r)}},y_{n_{(r)}}\right)\right]\right\}}, \quad R=s-1 \tag{8}$$

$$y^{(q)}\left\{\begin{array}{c} re \\ im \end{array}\right\}_{(s-1)} = \frac{\sum_{r=1}^{R}\sum_{n_{(r)}=1}^{N_{(r)}}\left\{y_{n_{(r)}}^{(q)}\left\{\begin{array}{c} Re \\ Im \end{array}\right\}\left[\tau_{dn}^{(q)}\left(x_{n_{(r)}},y_{n_{(r)}}\right)\right]\right\}}{\sum_{n_{(r)}=1}^{N_{(r)}}\left\{\left\{\begin{array}{c} Re \\ Im \end{array}\right\}\left[\tau_{dn}^{(q)}\left(x_{n_{(r)}},y_{n_{(r)}}\right)\right]\right\}} \tag{9}$$

and side, $L_{(s-1)}^{(q)}$, of the squared occupation-ares

$$L_{(s-1)}^{(q)} = \frac{L_{re}^{(q)}{}_{(s-1)} + L_{im}^{(q)}{}_{(s-1)}}{2} \tag{10}$$

being

$$L^{(q)}\left\{\begin{array}{c} re \\ im \end{array}\right\}_{(s-1)} = 2\frac{\sum_{r=1}^{R}\sum_{n_{(r)}=1}^{N_{(r)}}\left\{\frac{\rho_{n_{(r)}c_{(s-1)}}^{(q)}\left\{\begin{array}{c} Re \\ Im \end{array}\right\}\left[\tau_{dn}^{(q)}\left(x_{n_{(r)}},y_{n_{(r)}}\right)\right]}{max_{n_{(r)}=1,..,N_{(r)}}\left\{\left\{\begin{array}{c} Re \\ Im \end{array}\right\}\left[\tau_{dn}^{(q)}\left(x_{n_{(r)}},y_{n_{(r)}}\right)\right]\right\}}\right\}}{\sum_{r=1}^{R}\sum_{n_{(r)}=1}^{N_{(r)}}\left\{\frac{\left\{\begin{array}{c} Re \\ Im \end{array}\right\}\left[\tau_{dn}^{(q)}\left(x_{n_{(r)}},y_{n_{(r)}}\right)\right]}{max_{n_{(r)}=1,..,N_{(r)}}\left\{\left\{\begin{array}{c} Re \\ Im \end{array}\right\}\left[\tau_{dn}^{(q)}\left(x_{n_{(r)}},y_{n_{(r)}}\right)\right]\right\}}\right\}} \quad q=1,...,Q \tag{11}$$

for each region, $D_{O(s-1)}^{(q)}$, of connected object-pixels are computed (by assuming that the

positions of the discontinuities of the real and imaginary part of the object function be the same, as usually happens in physical situations of interest) in order to perform the synthetic zoom.

2.2 Retrieval Procedure

According to a multi-resolution strategy, an higher resolution level ($R = s$) is adopted only for the reduced investigation domains, $D^{(q)}_{O(s-1)}$, $q = 1, ..., Q_{(s)}$, where the *clustering procedure* estimated the presence of Q different objects. Then the dielectric profile is retrieved by minimizing the multi-object multi-resolution cost function, $\Phi^{(s)}$

$$\Phi^{(s)}\left\{\tau^{(s)}_{(q)}\left(x_{n_{(r)}}, y_{n_{(r)}}\right),\ E^{v\,(s)}_{tot}\left(x_{n_{(r)}}, y_{n_{(r)}}\right);\ \begin{array}{cc} q=1,..,Q_{(s)}; & r=1,...,R=s; \\ n_{(r)}=1,...,N_{(r)}; & v=1,...,V \end{array}\right\} =$$
$$\left\{\sum_{q=1}^{Q_{(s)}}\sum_{v=1}^{V}\sum_{m_{(v)}=1}^{M_{(v)}}\left|E^{v}_{scatt}\left(x_{m_{(v)}}, y_{m_{(v)}}\right) - \sum_{r=1}^{R}\sum_{n_{(r)}=1}^{N_{(r)}}\left\{w^{(q)}\left(x_{n_{(r)}}, y_{n_{(r)}}\right)\tau^{(s)}_{(q)}\left(x_{n_{(r)}}, y_{n_{(r)}}\right)\right.\right.$$
$$\left.\left.E^{v\,(s)}_{tot}\left(x_{n_{(r)}}, y_{n_{(r)}}\right)G_{2d}\left(A_{n_{(r)}}, \rho_{n_{(r)}m_{(v)}}\right)\right\}\right|^2\Bigg\} + \Bigg\{\sum_{q=1}^{Q_{(s)}}\sum_{v=1}^{V}\sum_{r=1}^{R}\sum_{n_{(r)}=1}^{N_{(r)}}$$
$$\left\{w^{(q)}\left(x_{n_{(r)}}, y_{n_{(r)}}\right)\left|E^{v}_{inc}\left(x_{n_{(r)}}, y_{n_{(r)}}\right) - \left[E^{v\,(s)}_{tot}\left(x_{n_{(r)}}, y_{n_{(r)}}\right)\right.\right.$$
$$\left.\left.+\sum_{u_{(r)}=1}^{N_{(r)}}\left\{\tau^{(s)}_{(q)}\left(x_{u_{(r)}}, y_{u_{(r)}}\right)\ \ E^{v\,(s)}_{tot}\left(x_{u_{(r)}}, y_{u_{(r)}}\right)G_{2d}\left(A_{u_{(r)}}, \rho_{u_{(r)}n_{(r)}}\right)\right\}\right]\right|\Bigg\}^2\Bigg\} \tag{12}$$

where

$$w^{(q)}(x_{n_{(r)}}, y_{n_{(r)}}) = \begin{cases} 0\ if\ \ (x_{n_{(r)}}, y_{n_{(r)}})\ \notin D^{(q)}_{O(s-1)} \\ 1\ if\ \ (x_{n_{(r)}}, y_{n_{(r)}})\ \in D^{(q)}_{O(s-1)} \end{cases}$$

and assuming that $Q_{(s=0)} = 1$.

Because of the multi-scaling method is no dependent on the definition of the cost function or the minimization algorithm, actually the optimization procedure constitutes a "*black box*" inside the overall system and, for simplicity, a conjugate-gradient optimizer based on the alternating direction implicit method [13] (CGADIM) is used. Contrary to the modified gradient method [14], where the unknown fields and contrast are updated simultaneously, but similarly to the contrast source inversion method [15], $\underline{\tau}^{(s)}_k = \left\{\left[\tau^{(s)}_{(q)}\left(x_{n_{(r)}}, y_{n_{(r)}}\right)\right]_k;\ \ q = 1,..,Q_{(s)};\ \ r = 1,...,R = s;\ \ n_{(r)} = 1,...,N_{(r)}\right\}$ and $\underline{E}^{(s)}_k =$

$\left\{\left[E_{tot}^{v\,(s)}\left(x_{n_{(r)}}, y_{n_{(r)}}\right)\right]_k;\ r=1,...,R=s\,;\ n_{(r)}=1,...,N_{(r)};\ v=1,...,V\right\}$ are iteratively (k being the iteration number) reconstructed by alternatively updating the two sequences. At each step of the multi-scaling procedure, the minimization algorithm is stopped when a maximum number of iterations, K (i.e., $k \leq K$), or a threshold on the cost function value, δ (i.e., $\Phi^{(s)}\left\{\underline{\tau}_k^{(s)}, \underline{\underline{E}}_k^{(s)}\right\} \leq \delta$), or the value of the cost function remain unaltered in a fixed percentage of the total amount of minimization-algorithm iterations (i.e., $\frac{\left|K_w \Phi^{(s)}\left\{\underline{\tau}_k^{(s)}, \underline{\underline{E}}_k^{(s)}\right\} - \sum_{h=1}^{K_w}\left[\Phi^{(s)}\left\{\underline{\tau}_h^{(s)}, \underline{\underline{E}}_h^{(s)}\right\}\right]\right|}{\Phi^{(s)}\left\{\underline{\tau}_k^{(s)}, \underline{\underline{E}}_k^{(s)}\right\}} \leq \varsigma$, K_w being an integer number).

2.3 Termination Procedure

The multi-resolution procedure is iterated until a "stationary condition" for the iterative procedure ($s = 1, ...S$) is achieved ($S = S_{opt}$ being the final step) in each of the Q regions defined by the *clustering procedure*. This condition holds when

- the number of regions identified by the clustering procure is stationary, then

$$\frac{\sum_{r=1}^{s}\left\{\left|Q_{(s)} - Q_{(r)}\right|\right\}}{s} < \eta_Q \tag{13}$$

- the qualitative-reconstruction parameters are stable, that is

$$\begin{aligned} min_{q=1,..,Q_{(s)}}\left\{\eta_x^{(s)}\right\}_{(q)} &< \eta_x \\ min_{q=1,..,Q_{(s)}}\left\{\eta_y^{(s)}\right\}_{(q)} &< \eta_y \\ min_{q=1,..,Q_{(s)}}\left\{\eta_L^{(s)}\right\}_{(q)} &< \eta_L \end{aligned} \tag{14}$$

being $\left\{\eta_u^{(s)}\right\}_{(q)} = \left\{\frac{\left|u_{c_{(s+1)}}^{(q)} - u_{c_{(s)}}^{(q)}\right|}{\left|u_c^{(s+1)}\right|} \times 100\right\}$, $u = x, y, L$ and where η_u, $u = x, y, L, Q$ are fixed thresholds.

3 Numerical Validation

In the following, the capabilities and current limitations of the IMM to localize, shape and reconstruct multiple dielectric scatterers, are assessed by means of several numerical simulations. The numerical validation is composed of two parts. Firstly, some tests with synthetically-generated data (Subsection 3.1) are performed in order to evaluate different noisy conditions as well as scatterer number and properties. Then, in Subsection 3.2, the IMM is checked in correspondence with experimentally-acquired data.

Concerning the numerical examples, the investigation domain, D_I, consists of a square with sides of length ℓ, while the measurement domain, D_M, is a circle subdivided in equally-spaced arcs whose mid-point serves as the location of a receiver. The data-acquisition configuration is a multi-illumination-angle/multi-view system [17].

As far as the IMM is concerned, the following parametric configuration has been heuristically (after an exhaustive set of numerical experiments) chosen: $\eta_x = \eta_y = 2\,\%$, $\eta_L = 5\,\%$, $\eta_Q = 0.5$, and T_τ is equal to the value of the global minimum of the envelope of the grey-level image histogram in the range $(0.2\tau_{max}, 0.8\tau_{max})$ (as an example, $T_\tau = 0.25$ in Fig. $2(b)$). On the other hand, the parameters values for the optimization algorithm resulted: $K = 2000$, $\delta = 10^{-4}$, $K_w = 100$, and $\varsigma = 10^{-2}$.

3.1 Testing against Synthetic-Data

In all the examples presented in this sub-section, the scatterering configuration is assumed to be enclosed in an investigation domain $\ell = 4\,\lambda$-sided (λ being the free-space wavelength) and illuminated by a set of $V = 8$ unit TM plane waves impinging at $\theta_{inc}^v = (v-1)\frac{\pi}{2}$, $v = 1, ..., V$. For each illumination, the scattered electric field data have been collected at $M_{(v)} = M$, $v = 1, ..., V$, (being M chosen according to the indications reported in [1] and aimed at collecting all the available information of the scenario under test) sensors located on the circular observation domain $\rho_m^\nu = 2.94\,\lambda$ in radius. Data values are numerically computed by using the Richmond's procedure [18] with a proper discretization (different

from that used at each step of the IMM) of the investigation domain in order to prevent the "inverse crime" problem.

As a first experiment, aimed at highlighting the effectiveness of the IMM in locating multiple objects without prior knowledge of the number, locations, or sizes in noiseless as well in noisy conditions, the retrieval of a scattering object constituted by two lossless homogeneous ($\tau_{(q)}(x,y) = 0.5$, $q = 1, 2$) cylinders, located at ($x_c^{(1)} = 0.67\,\lambda$, $y_c^{(1)} = 0.67\,\lambda$), ($x_c^{(2)} = -0.67\,\lambda$, $y_c^{(2)} = -0.67\,\lambda$), and $L^{(q)} = 0.67\,\lambda$ in side, is considered.

Figure 3 shows the dielectric distributions retrieved at different steps of the multi-scaling process. The actual profile is also reported in Figure 3(a) and, in the reconstructed profiles (Figs. 2(b)-(c)), the dashed line indicates the regions occupied by actual structures. As can be observed, starting from the free-space configuration, the IMM sequentially identifies two regions in the investigation domain (Fig. 2(b)), and successively refines the reconstruction of each object ending the process with the estimate of Fig. 2(c). The increase of the qualitative and quantitative imaging effectiveness during the multi-step process is also confirmed by the values of the error figures reported in Tab. I and computed according to the following expressions

$$\rho^{(q)} = \frac{\sqrt{\left[x_{c_{(S_{opt})}}^{(q)} - x_c^{(q)}\right]^2 + \left[y_{c_{(S_{opt})}}^{(q)} - y_c^{(q)}\right]^2}}{\lambda} \quad q = 1, ..., Q_{(S_{opt})} \tag{15}$$

$$\Delta^{(q)} = \left\{ \frac{\left| L_{(S_{opt})}^{(q)} - L^{(q)} \right|}{L^{(q)}} \right\} \times 100 \quad q = 1, ..., Q_{(S_{opt})} \tag{16}$$

$$\xi \left\{ \begin{array}{c} re \\ im \end{array} \right\}^{(j)} = \sum_{r=1}^{R} \frac{1}{N_{(r)}^{(j)}} \sum_{n_{(r)}=1}^{N_{(r)}^{(j)}} \left\{ \frac{\left\{ \begin{array}{c} Re \\ Im \end{array} \right\} \left[\tau^{(S_{opt})}\left(x_{n_{(r)}}, y_{n_{(r)}}\right) \right] - \left\{ \begin{array}{c} Re \\ Im \end{array} \right\} \left[\tau^{ref}(x_{n_{(r)}}, y_{n_{(r)}}) \right]}{\left\{ \begin{array}{c} Re \\ Im \end{array} \right\} \left[\tau^{ref}(x_{n_{(r)}}, y_{n_{(r)}}) \right]} \right\} \times 100 \quad R = S_{opt} \tag{17}$$

τ^{ref} being the actual object function and the index $N_{(r)}^{(j)}$ can range over the whole investi-

gation domain ($j \Rightarrow tot$), or over the area where the q-th actual object is located ($j \Rightarrow_{int}^{(q)}$), or over the background belonging to the investigation domain ($j \Rightarrow ext$);

To evaluate the effect of the measurement noise on the reconstruction capabilities of the method, the noise has been simulated by adding to the scattered data a complex Gaussian random variable with zero mean value and a standard deviation given by

$$\chi = \frac{\sum_{\nu=1}^{V} \sum_{m_{(v)}=1}^{M_{(v)}} \left| E_{scatt}^{v}\left(x_{m_{(v)}}, y_{m_{(v)}}\right) \right|^2}{2MV(SNR)} \tag{18}$$

SNR being the signal-to-noise ratio. Figure 4 shows the results achieved at the stopping step of the IMM for different signal-to-noise-ratio values ranging from $SNR = 20\,dB$ to $SNR = 5\,dB$. As expected, the presence of the noise causes a deterioration of the reconstruction accuracy as confirmed from the error figures given in Tab. II. Intuitively, it can be expected that as the signal power reduces, it will be increasingly difficult to recover higher-order information about the target structure and an high resolution level. Consequently, when the noise increase also a reconstruction-noise appears and for very high noise level ($SNR = 5\,dB$) multiple, false structures can be observed near the right objects. However, it should be pointed out that for $SNR > 5\,dB$ the obtained reconstructions appear satisfactory in term of location, shaping and also dielectric-distribution estimation.

Then, in the the second experiment, we turn our attention to a more challenging problem, in which the scattering objects present also a conductivity equal to $\sigma_{(q)}(x, y) = 0.1\,[S/m]$, $q = 1, 2$. The geometric configuration is the same as in the previous example in order to correctly evaluate the impact of the conductivity on the reconstruction accuracy.

As well as for the lossless case, the IMM is effective in detecting and locating multiple objects (Fig. 5) and with the decrease of the signal-to-noise ratio also the reconstruction accuracy reduces producing larger errors inside the actual-scatterer regions (also in comparison with those produced in the lossless case: $13.30 \leq \left[\xi_{int}^{(1)}\right]_{\sigma=0.1} \leq 33.34$ versus $8.56 \leq \left[\xi_{int}^{(1)}\right]_{\sigma=0.0} \leq 9.90$ and $7.11 \leq \left[\xi_{int}^{(2)}\right]_{\sigma=0.1} \leq 33.30$ versus $7.73 \leq \left[\xi_{int}^{(1)}\right]_{\sigma=0.0} \leq 16.11$)

Tab. III. However, it should be pointed out that for high SNR values, even if the shape of the two scatterers cannot be exactly identified, the algorithm converge to a structure that occupies a large area of the actual one.

For completeness, Figure 6 gives the behavior of the multi-scaling cost function during the optimization process for the noiseless case (presenting also the decrease in the state and data terms) and for different noisy conditions. From Fig. $6(a)$, it can be observed that, due to the free-space initialization, $\left[\Phi^{(1)}_{State}\right]_{k=0} = 0$ and, at the first iterations, the cost function is largely dependent from the data term, $\Phi^{(1)}_{Data}$. With the increase of the iteration number, for different steps ($s = 1, 2, 3$) of the multi-scaling procedure, the optimization algorithm proceeds into the minimization of the two terms whose amplitudes result almost comparable. On the other hand, Fig. $6(b)$ clearly points out that the minimization results more difficult in correspondence with an increase of the SNR value justifying the reduction of the reconstruction accuracy shown in Fig. $5(c)$ (and also in Fig. $4(c)$) and confirmed by numerical values in Tab. III.

A further assessment of the IMM is performed by considering the dielectric distribution shown in Fig. $7(a)$ ($\tau_{(1)}(x, y) = 0.5$, $\tau_{(2)}(x, y) = 1.0$) and noisy data ($SNR = 15\,dB$). In order to point out the advantages of the iterative multi-scaling strategy over standard iterative approaches (which does not perform a multi-scaling/multi-resolution process but directly process the inverse scattering data), the reconstruction has been carried out by using also an iterative single-step approach (ISSM) based on the conjugate-gradient alternating direction implicit method (i.e., the same optimizer used during the *retrieval procedure* of the IMM). As far as the discretization of the investigation domain used by the single-step approach is concerned, an homogeneous discretization with a cell-side equal to the finer discretization step of the multi-scaling procedure is adopted. As far as the IMM is concerned, the same level of performances as it can be seen in the previous example results also here. On the contrary, the use of the ISSM leads to a reconstruction much worse in term of localization accuracy ($\frac{\rho^{(1)}_{ISSM}}{\rho^{(1)}_{IMM}} = 4.76$ and $\frac{\rho^{(2)}_{ISSM}}{\rho^{(2)}_{IMM}} = 2.70$). Moreover, the poor estimate of the contrast function for the object on the left-bottom region of the

investigation domain ($max_{(x,y)\in D_O^{(2)}}\left\{\tau_{(2)}^{ISSM}(x,y)\right\} = 0.4$ and $av_{(x,y)\in D_O^{(2)}}\left\{\tau_{(2)}^{ISSM}(x,y)\right\} = 0.24$) and the presence of small artifacts in the region near the actual objects, produces significant errors in the quantitative error figures (Tab. IV) as well as in estimating the objects dimensions ($\frac{\Delta_{ISSM}^{(1)}}{\Delta_{IMM}^{(1)}} = 4.02$ and $\frac{\Delta_{ISSM}^{(2)}}{\Delta_{IMM}^{(2)}} = 3.07$).

This example points out a typical feature of the IMM that is the capability of the approach to zoom on the reconstructed image achieving a great accuracy in determining the correct value of the contrast function (being $max_{(x,y)\in D_O^{(1)}}\left\{\tau_{(1)}^{IMM}(x,y)\right\} = 0.65$, $av_{(x,y)\in D_O^{(1)}}\left\{\tau_{(1)}^{IMM}(x,y)\right\} = 0.49$ and $max_{(x,y)\in D_O^{(2)}}\left\{\tau_{(2)}^{IMM}(x,y)\right\} = 1.1$, $av_{(x,y)\in D_O^{(2)}}\left\{\tau_{(2)}^{IMM}(x,y)\right\} = 1.01$).

In the last synthetic example, aimed at evaluating the dependence of the reconstruction on the number of objects inside the investigation domain, three lossless square cylinders ($\tau_{(q)}(x,y) = 0.5$, $q = 1,2,3$) centered at (($x_c^{(1)} = 0.67\,\lambda$, $y_c^{(1)} = 0.67\,\lambda$), ($x_c^{(2)} = -0.67\,\lambda$, $y_c^{(2)} = 0.67\,\lambda$), and ($x_c^{(3)} = 0.0$, $y_c^{(1)} = -0.67\,\lambda$)) and $L^{(q)} = 0.67\,\lambda$-sided are considered (Fig. 8 (a)). In correspondence of a noisy environment, characterized by a $SNR = 15\,dB$, the IMM is able to achieve the reconstructed distribution shown in Fig. 8(b). It can be noted that the approach keeps its effectiveness in discrimining and locating different objects (as confirmed by the values of the localization error: $\rho^{(1)} = 0.012$, $\rho^{(2)} = 0.023$, and $\rho^{(2)} = 0.013$). Also the estimated contrast value results very close to the expected one as well as the homogeneous behavior of the contrast function ($\xi_{int}^{(1)} = 5.45$, $\xi_{int}^{(2)} = 4.57$, and $\xi_{int}^{(3)} = 5.95$).

3.2 Testing against Real-Data

Finally, the last experiment is concerned with the reconstruction of a multiple-scatterers configuration starting from real-scattered data belonging to the "Marseille" dataset [16]. In particular, the considered data ("dielTM_8f.exp") are related to two filled dielectric cylinders characterized by a relative permittivity equal to $\varepsilon_r(x,y) = 3.0 \pm 0.3$, $(x,y) \in D_O^{(q)}$, $q = 1,2$ (corresponding to an object function $\tau_{(q)}(x,y) = 2.0 \pm 0.3$, $q = 1,2$) with circular cross-sections $a = 15\,mm$ in radius and placed about $30\,mm$ from the center of the

experimental setup ($d = 90\,mm$ being the distance between the centers of the cylinders). A detailed description of the underlying experimental setup as well as the data sets is given in the introduction of [16] (pp. 1565-1572) by Belkebir and Saillard.

In order to perform the reconstruction, the IMM has been applied to monochromatic datasets at $f = 4\,GHz$ ($\frac{a}{\lambda} = 0.2$, $\frac{d}{\lambda} = 1.2$) and the investigation domain has been chosen to be a squared area of $30 \times 30\,cm^2$ ($\frac{\ell}{\lambda} = 4.0$). Due to the *aspect-limited* nature of the scattered data (the measures are not acquired in an angular sector of 60^o), the information available from the scattered data results strongly reduced. Consequently, the complete data-set ($V = 36$ and $M = 49$) is processed by the IMM.

As far as the multi-illumination/multi-view system of the experimental setup is concerned, the fields are generated and received by double-ridged horn antennas. Since the data equation (2) is based on the knowledge of the incident fields and the design of the set-up does not provide such information (but only the field in absence of the target as measured on the observation domain), transmitting antennas have been approximated by line sources parallel to the cylindrical scatterers.

Figure 9 shows a typical evolution of the reconstructed profile during the multi-step procedure and the corresponding behavior of the cost function as a function of the number of iterations (Fig. $9(d)$). Starting from a free-space dielectric profile and field distribution, Fig. $9(a)$ shows the object-function distribution retrieved at $s = 1$. As can be observed, some artifacts are present in the investigation domain and neither an accurate qualitative nor quantitative imaging of the actual objects is achieved. Consequently, the clustering procedure identifies only one region ($Q_{(s)} = 1$, $s = 1$) located at $x^{(1)}_{c_{(1)}} = 0.102\,\lambda$, $y^{(1)}_{c_{(1)}} = 7 \times 10^{-3}\,\lambda$, $L^{(1)}_{(1)} = 1.617\,\lambda$ in side, where "a scatterer" is present. At the end of second step ($s = 2$), the algorithm achieves the *splitting step* where the *clustering procedure* is able to define two smaller regions ($Q_{(2)} = 2$) where two not-connected objects are located at the positions $\left(x^{(1)}_{c_{(2)}} = 0.172\,\lambda,\, y^{(1)}_{c_{(2)}} = 0.589\,\lambda\right)$ ($L^{(1)}_{(2)} = 0.498\,\lambda$-sided) and $\left(x^{(2)}_{c_{(2)}} = 3 \times 10^{-2}\,\lambda,\, y^{(2)}_{c_{(2)}} = -0.634\,\lambda\right)$ ($L^{(2)}_{(2)} = 0.517\,\lambda$-sided), respectively. The two cylinders appear correctly localized, slightly overestimated and

fairly well retrieved (Fig. 9(b)). The optimal dielectric profile, $\underline{\tau}^{(S_{opt})}$, $S_{opt} = 3$, is then given in Figure 9(c). The resolution accuracy further improves in term of localization ($(x_{c_{(2)}}^{(1)} = 0.116\,\lambda$, $y_{c_{(2)}}^{(1)} = 0.604\,\lambda$, $L_{(2)}^{(1)} = 0.436\,\lambda$), ($(x_{c_{(2)}}^{(2)} = -0.018\,\lambda$, $y_{c_{(2)}}^{(2)} = -0.614\,\lambda$, $L_{(2)}^{(2)} = 0.437\,\lambda$)) as well as as quantitative estimation of the dielectric distribution (being $max_{(x,y)\in D_O^{(1)}}\left\{\tau_{(1)}^{(S_{opt})}(x,y)\right\} = 2.2$, $av_{(x,y)\in D_O^{(1)}}\left\{\tau_{(1)}^{(S_{opt})}(x,y)\right\} = 2.09$ and $max_{(x,y)\in D_O^{(2)}}\left\{\tau_{(2)}^{(S_{opt})}(x,y)\right\} = 2.1$, $av_{(x,y)\in D_O^{(2)}}\left\{\tau_{(2)}^{(S_{opt})}(x,y)\right\} = 2.04$). For comparison purposes, Figure 10 shows the image of the dielectric profile reconstructed by means of the ISSM with the same resolution level achieved by the multi-scaling procedure. The retrieved profile presents some artifacts (producing an overestimation of the dimensions of the scatterers ($L_{ISSM}^{(1)} = 0.777\,\lambda$, $L_{ISSM}^{(2)} = 0.626\,\lambda$) as well as an incorrect localization ($x_{c_{ISSM}}^{(1)} = -0.014\,\lambda$, $y_{c_{ISSM}}^{(1)} = 0.770\,\lambda$) and ($x_{c_{ISSM}}^{(2)} = 0.033\,\lambda$, $y_{c_{ISSM}}^{(1)} = -0.774\,\lambda$)) and the homogeneity of the two objects is lost. Moreover, inside the regions where the actual objects are located, the value of the contrast is far from the expected one with maximum value ($max_{(x,y)\in D_O^{(1)}}\left\{\tau_{(1)}^{ISSM}(x,y)\right\} = 1.67$, $max_{(x,y)\in D_O^{(2)}}\left\{\tau_{(2)}^{ISSM}(x,y)\right\} = 1.58$).

4 Conclusions and Future Developments

The retrieval of cross-sectional distribution of multiple cylindrical objects located in free space has been performed via the iterative multi-scaling method. Theoretical and algorithmic details on the solution method for multiple scatterers imaging have been presented and validated by means of numerical experiments. Selected examples, dealing with noisy-synthetic data as well as experimentally-acquired measures, have been presented assessing the effectiveness but also current limitations of the proposed procedure.

As far as the current limitations of the IMM are concerned, certainly they are due to two main reasons:

- the use of a "black box" optimization algorithm which in principle, without an accurate analysis of the cost function or a lot of *a-priori* knowledge of the problem, could be trapped in local minima corresponding to wrong reconstruction of the

dielectric profile;

- the use of a simple *clustering procedure* in order to estimate the number of scatterers belonging to the investigation domain.

In order to overcome these drawbacks some possible solutions (subject of future researches) could be a minimization performed by means of a global optimization procedure able to avoid local minima in the solution-space sampling procedure and computationally effective also in a serial implementation in correspondence with a low dimension search-space (as that considered at each step of the IMM). On the other hand, more sophisticated clustering methodologies (see [19] and the references therein for a general overview) also based on electromagnetic criteria would greatly improve the reconstruction accuracy of the IMM increasing the convergence rate of the minimization algorithm and avoiding some artifacts occurring especially in high-noise environments. Moreover, further refinements could be achieved with the use of region-based approaches such as region growing by split-and-merge techniques broadly used in image processing and currently under study for an application in microwave imaging applications.

References

[1] O. M. Bucci and G. Franceschetti, "On the degrees of freedom of scattered fields," *IEEE Trans. Antennas Propagat.*, vol. 37, pp. 918-926, 1989.

[2] A. J. Devaney, "Geophysical diffraction tomography," *IEEE Trans. Geosci. Remote Sensing*, vol. 22, pp. 3-13, 1984.

[3] J. Ch. Bolomey. *Frontiers in Industrial Process Tomography.* Engineering Foundation, 1995.

[4] J. Ch. Bolomey, "Microwave imaging techniques for NDT and NDE," *Proc. Training Workshop on Advanced Microwave NDT/NDE Techniques*, Supelec/CNRS, Paris, Sept. 7-9, 1999.

[5] E. L. Miller and A. S. Willsky, "A multiscale, statistically based inversion scheme for linearized inverse scattering problems," *IEEE Trans. Geosci. Remote Sensing*, vol. 34, pp. 346-357, 1996.

[6] E. L. Miller and A. S. Willsky, "Wavelet-based methods for nonlinear inverse scattering problem using the extended Born approximation," *Radio Sci.*, vol. 31, pp. 51-65, 1996.

[7] O. M. Bucci, L. Crocco, T. Isernia, and V. Pascazio, "Wavelets in non-linear inverse scattering," *Proc. Geoscience and Remote Sensing Symp.*, IGARSS-2000, vol. 7, pp. 3130-3132.

[8] O. M. Bucci, L. Crocco, and T. Isernia, "An adaptive wavelet-based approach for non destructive evaluation applications," *Proc. Antennas and Propagation Symp.*, APS-2000, vol. 3, pp. 1756-1759.

[9] S Caorsi, M. Donelli, and A. Massa, "An iterative multi-resolution approach for microwave imaging applications," *Microwave Optical Technol. Lett.*, vol. 32, pp. 352-356, 2002.

[10] S Caorsi, M. Donelli, D. Franceschini, and A. Massa, "A new methodology based on an iterative multiscaling for microwave imaging," *IEEE Trans. Microwave Theory Tech.*, vol. 51, pp. 1162-1173, 2003.

[11] D. Colton and R. Kress, *Inverse Acoustic and Electromagnetic Scattering Theory.* Springer, Berlin, 1992.

[12] D. S. Jones, *The Theory of Electromagnetism.* Oxford, U.K.: Pergamon Press, 1964.

[13] R. V. Kohn and A. McKenney, "Numerical implementation of a variational method for electrical impedance tomography," *Inverse Problems*, vol. 6, pp. 389-414, 1990.

[14] R. E. Kleinman and P. M. van den Berg, "A modified gradient method for two-dimensional problems in tomography," *J. Computat. Appl. Math.*, vol. 42, pp. 17-35, 1992.

[15] P. M. van den Berg and R. E. Kleinman, "A contrast source inversion method," *Inverse Problems*, vol. 13, pp. 1607-1620, 1997.

[16] K. Belkebir and M. Saillard, Special section: "Testing Inversion Algorithms against Experimental Data," *Inverse Problems*, vol. 17, pp. 1565-1702, 2001.

[17] S. Caorsi, G. L. Gragnani, and M. Pastorino, "An electromagnetic imaging approach using a multi-illumination technique," *IEEE Trans. Biomedical Eng.*, vol. 41, pp. 406-409, 1994.

[18] J. H. Richmond, "Scattering by a dielectric cylinder of arbitrary cross section shape," *IEEE Trans. Antennas Propagat.*, vol. 13, pp. 334-341, 1965.

[19] A. K. Jain, *Fundamentals of Digital Image Processing*. Englewood Cliffs, USA: Prentice-Hall, 1989.

Figure Caption

- Figure 1. Problem Geometry.

- Figure 2. An example of the *Clustering Procedure*. (a) Grey-level representation of reconstructed dielectric profile at s-th step, (b) binarized representation of the reconstructed dielectric profile after *thresholding*, $\tau_{th}(x_{n_{(r)}}, y_{n_{(r)}})$, (c) histogram of the reconstructed dielectric profile, (d) representation of the reconstructed dielectric profile after *filtering*, $\tau_{dn}(x_{n_{(r)}}, y_{n_{(r)}})$, and (e) neighborhood of pixel $(x_{n_{(r)}}, y_{n_{(r)}})$ in the pixel-labeling process.

- Figure 3. Iterative Process - Estimated permittivity distributions of two square homogeneous dielectric cylinders ($\tau_{(1)} = \tau_{(2)} = 0.5$) (Noiseless conditions). (a) Reference configuration. (b) $s = 1$, and (c) $s = S_{opt} = 2$.

- Figure 4. Estimated permittivity distributions of two square homogeneous dielectric cylinders ($\tau_{(1)} = \tau_{(2)} = 0.5$). Retrieved profile at $S = S_{opt}$ when: (a) $SNR = 20\,dB$, (b) $SNR = 10\,dB$, and (c) $SNR = 5\,dB$.

- Figure 5. Reconstruction of two square dissipative homogeneous cylinders ($\tau_{(1)} = \tau_{(2)} = 0.5 - j0.45$) (a). Retrieved profile at $S = S_{opt}$ when: (b) Noiseless conditions, (c) $SNR = 20\,dB$, (d) $SNR = 10\,dB$, and (e) $SNR = 5\,dB$.

- Figure 6. Iterative Process - Reconstruction of two square dissipative homogeneous cylinders ($\tau_{(1)} = \tau_{(2)} = 0.5 - j0.45$). Behavior of the Multi-Scaling Cost function for (a) noiseless and (b) noisy conditions.

- Figure 7. Reconstruction of two square homogeneous cylinders, characterized by different object functions ($\tau_{(1)} = 0.5$, $\tau_{(2)} = 1.0$) (a). Dielectric profile estimated by using (b) the IMM and (c) the ISSM for a $SNR = 15\,dB$.

- Figure 8. Reconstruction of three square homogeneous cylinders ($\tau_{(1)} = \tau_{(2)} = \tau_{(3)} = 0.5$). (a) Actual distribution and (b) retrieved profile in correspondence with noisy

($SNR = 15\,dB$) data.

- Figure 9. Iterative Process - Reconstruction of two square homogeneous cylinders (Real dataset "Marseille" [16] - "twodielTM_8f.exp"): (a) $s = 1$, (b) $s = 2$, and (c) $s = S_{opt} = 3$ (dashed line: actual profile). Behavior of the Multi-Scaling cost function (d).

- Figure 10. Reconstruction of two square homogeneous cylinders (Real dataset "Marseille" [16] - "twodielTM_8f.exp"). Retrieved profile with the ISSM.

Table Caption

- Table I. Two Lossless Dielectric Square Cylinders (Noiseless Conditions - Iterative Process) - Error Figures.
- Table II. Two Lossless Dielectric Square Cylinders (Noisy Conditions) - Error Figures.
- Table III. Two Dissipative Dielectric Square Cylinders (Noiseless and Noisy Conditions) - Quantitative (a) and Qualitative (b) Error Figures.
- Table IV. Two Lossless Dielectric Square Cylinders characterized by different object function ($SNR = 15\,dB$) - Comparison between the IMM and the CGADIM in term of Error Figures.

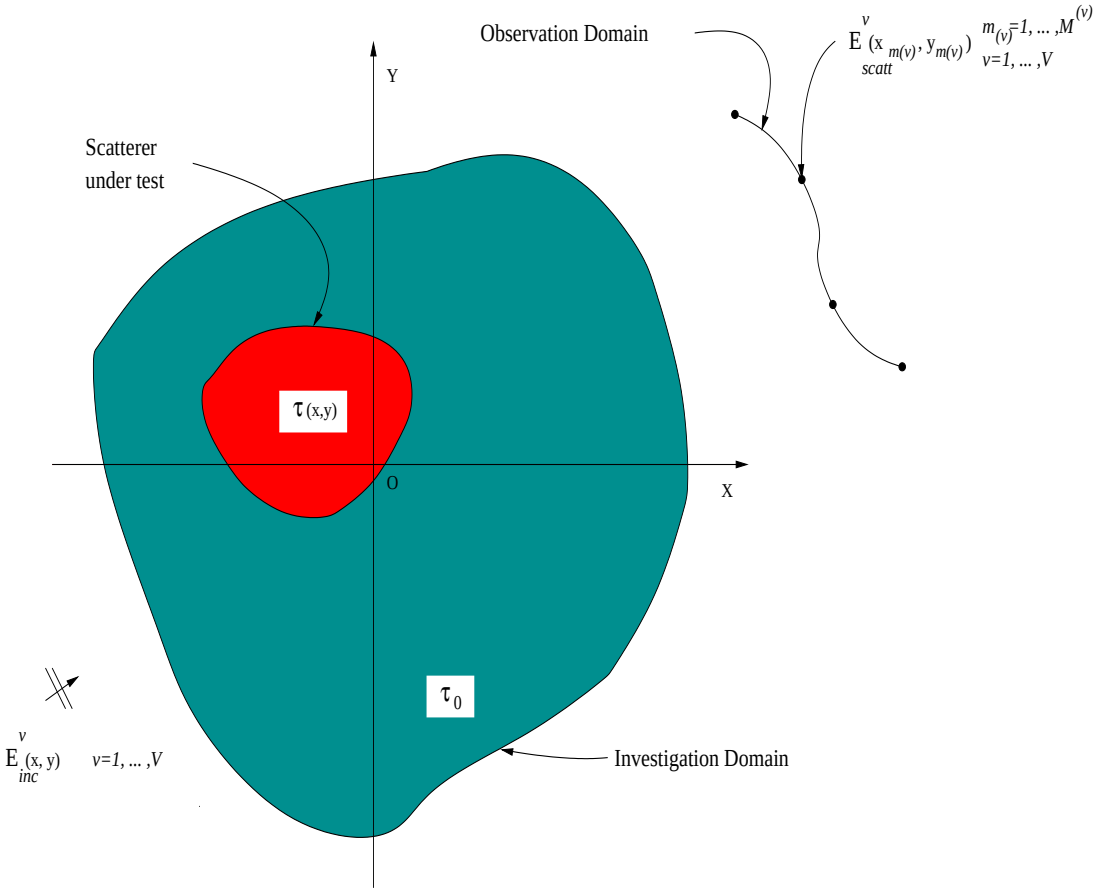

Fig. 1 - S. Caorsi *et al.*, "Detection and Imaging ..."

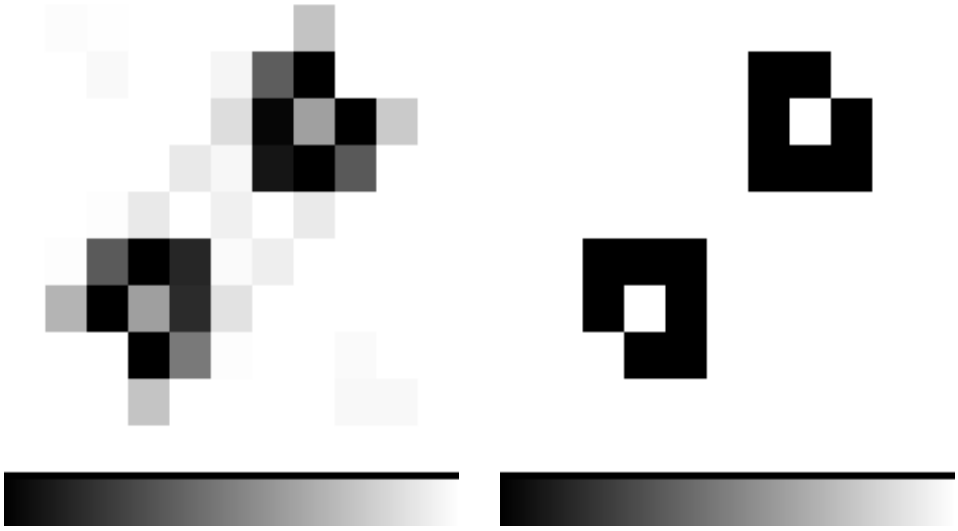

(a) (c)

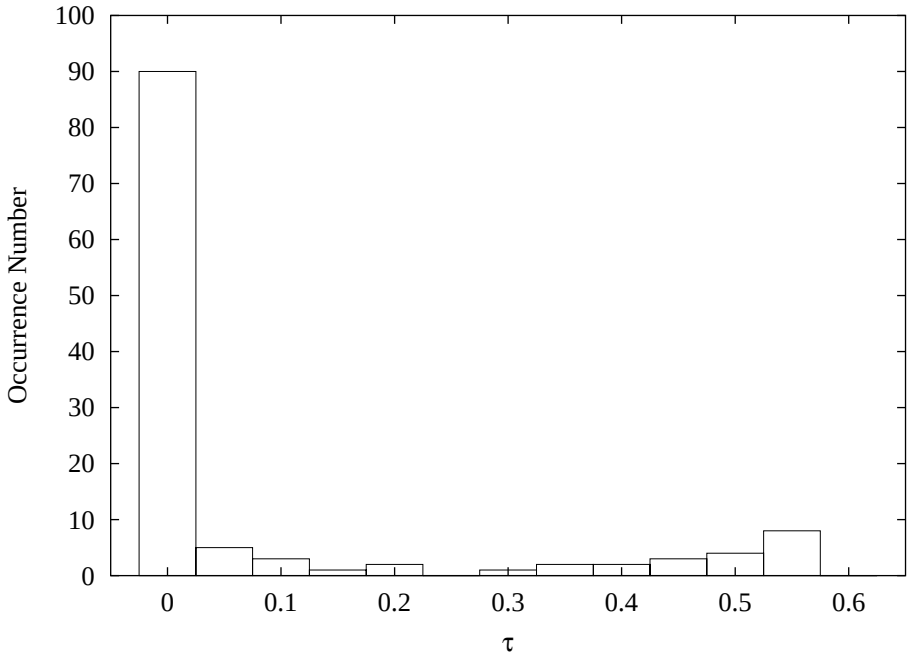

(b)

Fig. 2(I) - S. Caorsi *et al.*, "Detection and Imaging ..."

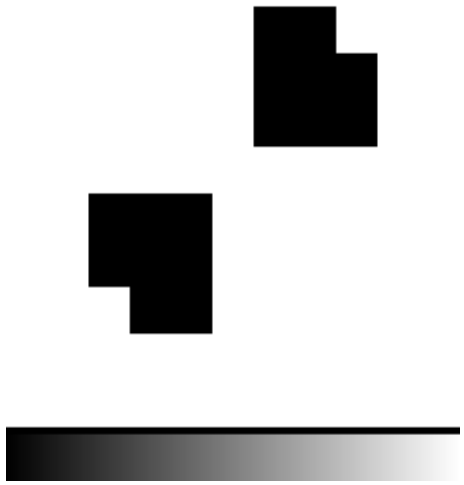

(d)

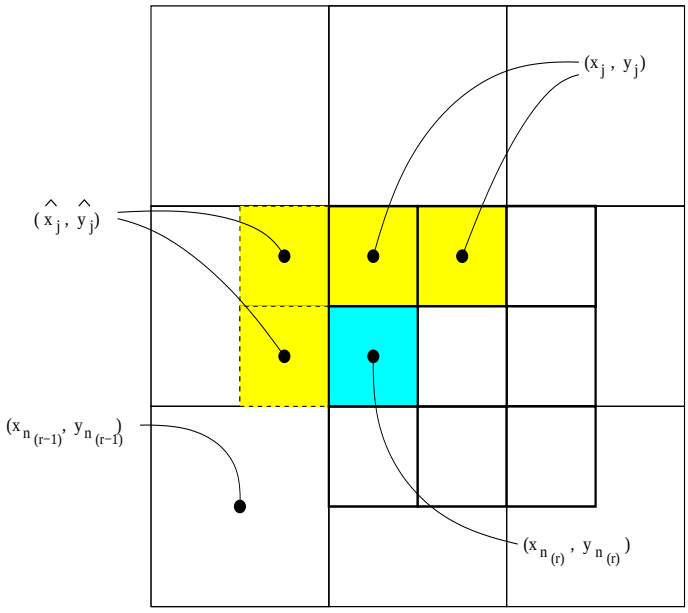

(e)

Fig. 2(*II*) - S. Caorsi *et al.*, "Detection and Imaging ..."

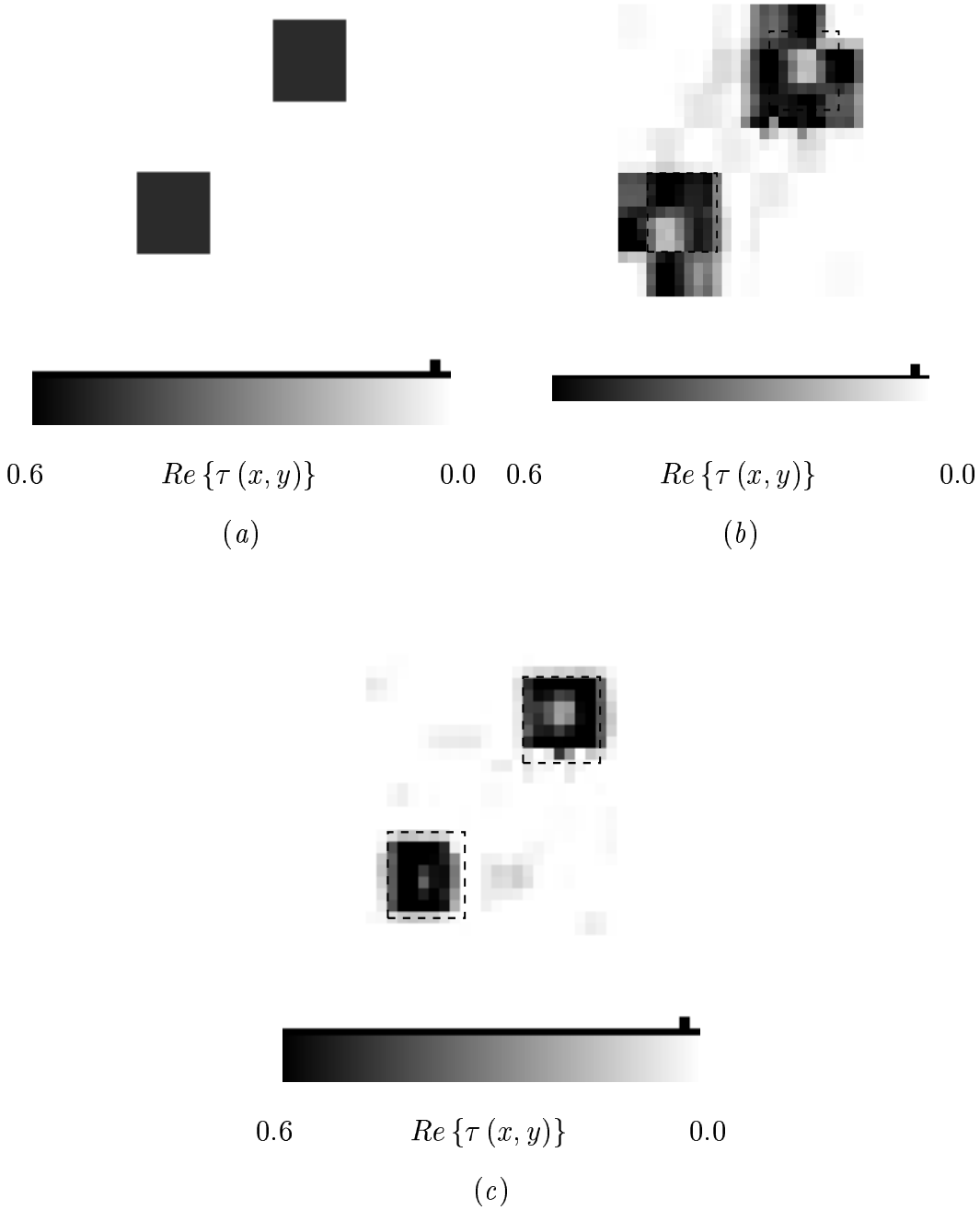

Fig. 3 - S. Caorsi *et al.*, "Detection and Imaging ..."

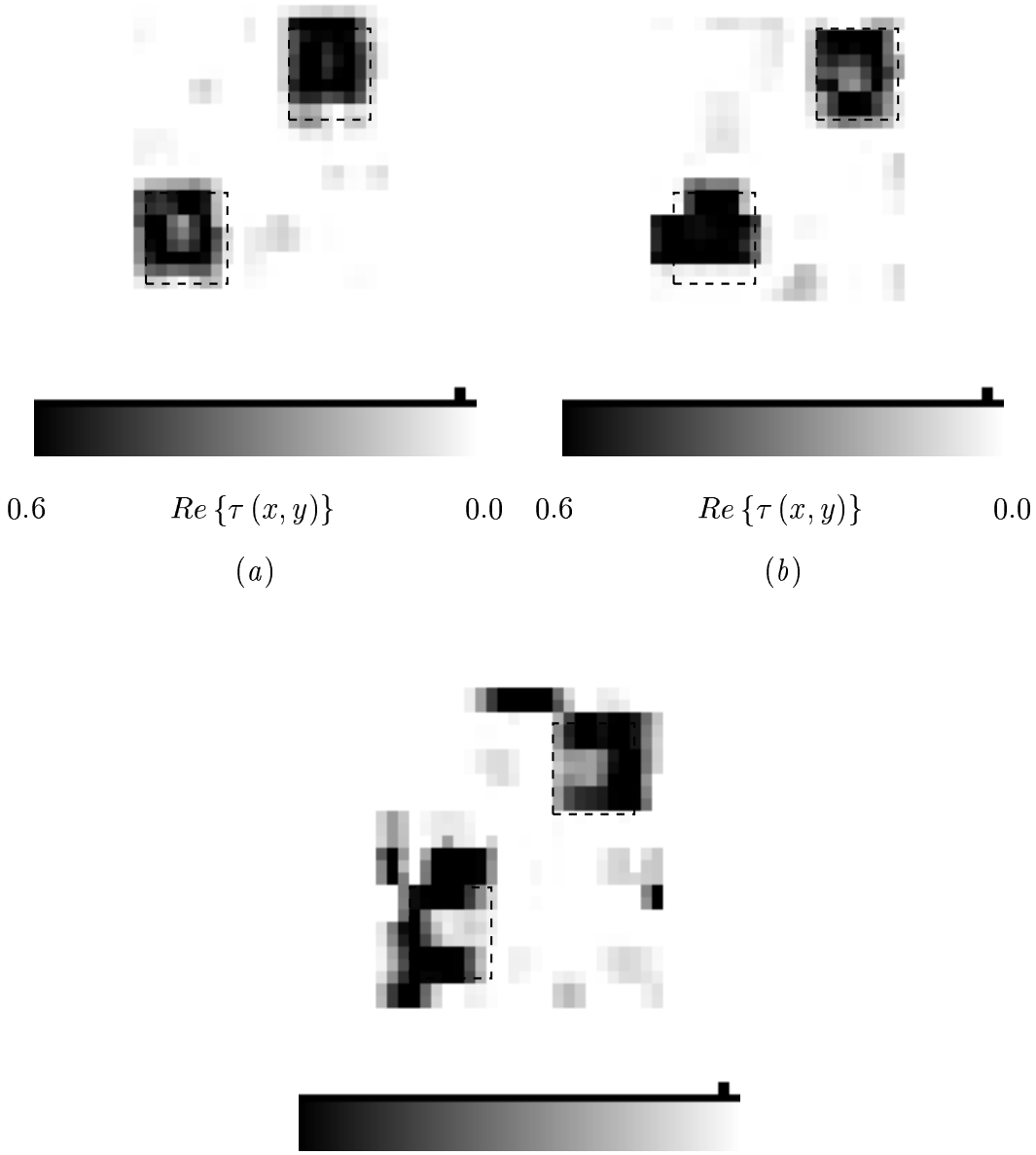

Fig. 4 - S. Caorsi *et al.*, "Detection and Imaging ..."

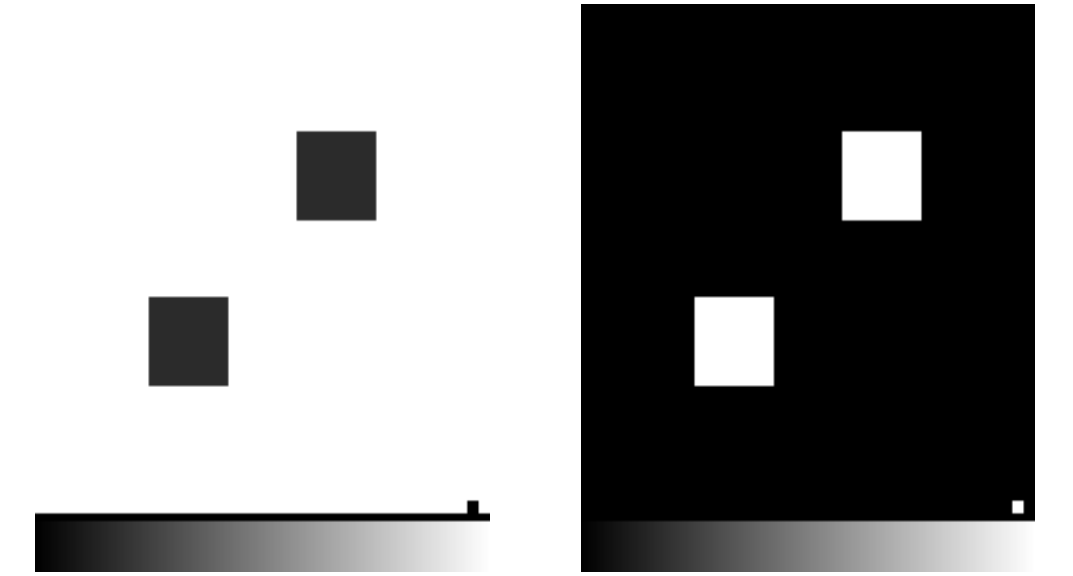

$0.6 \qquad Re\{\tau(x,y)\} \qquad 0.0 \quad 0.0 \qquad Im\{\tau(x,y)\} \qquad -0.47$

(a)

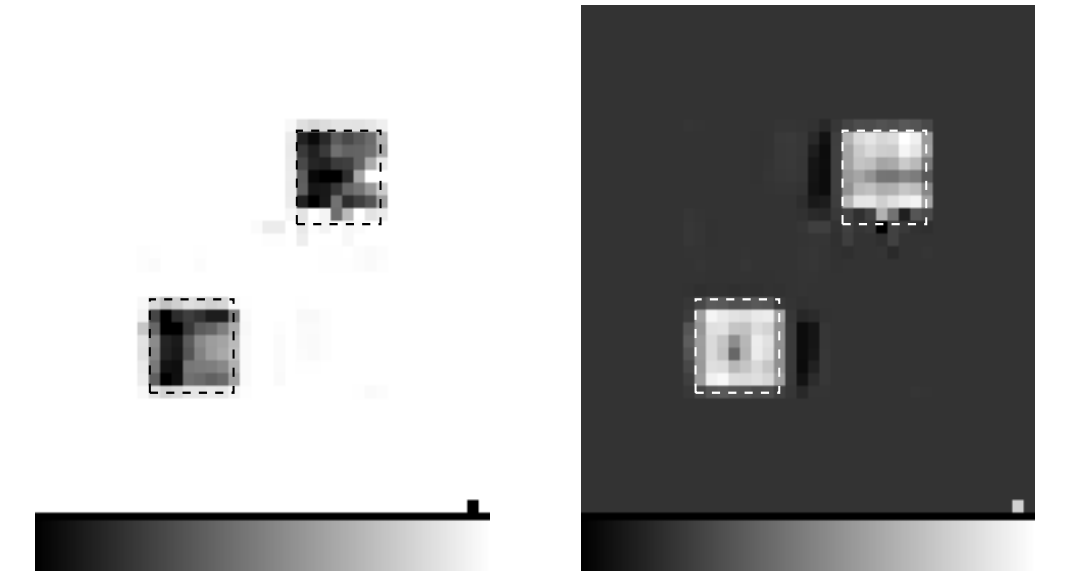

$0.6 \qquad Re\{\tau(x,y)\} \qquad 0.0 \quad 0.0 \qquad Im\{\tau(x,y)\} \qquad -0.47$

(b)

Fig. 5 (*I*) - S. Caorsi *et al.*, "Detection and Imaging ..."

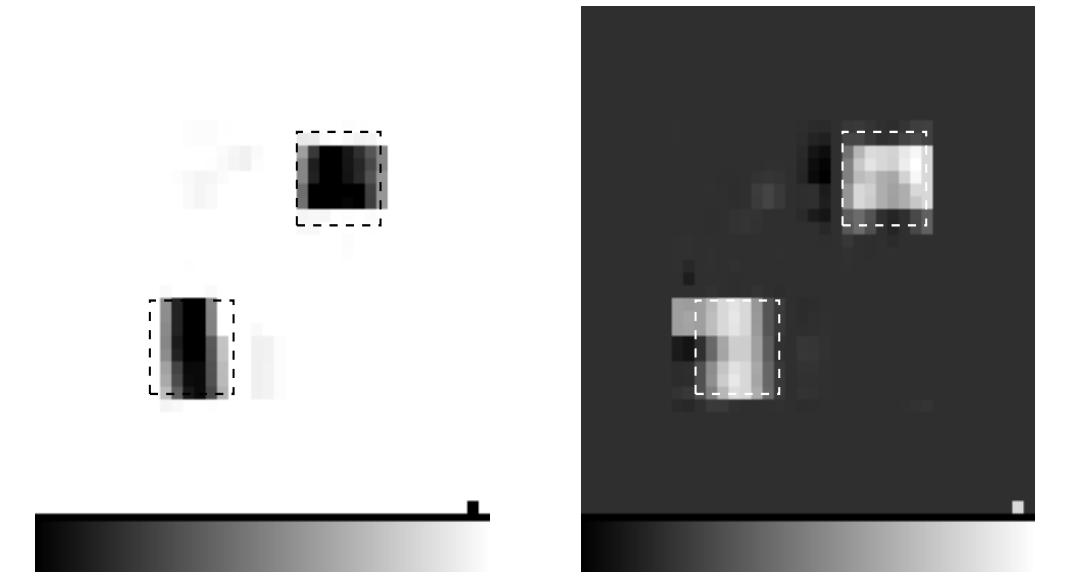

0.6 $Re\{\tau(x,y)\}$ 0.0 0.0 $Im\{\tau(x,y)\}$ -0.47

(c)

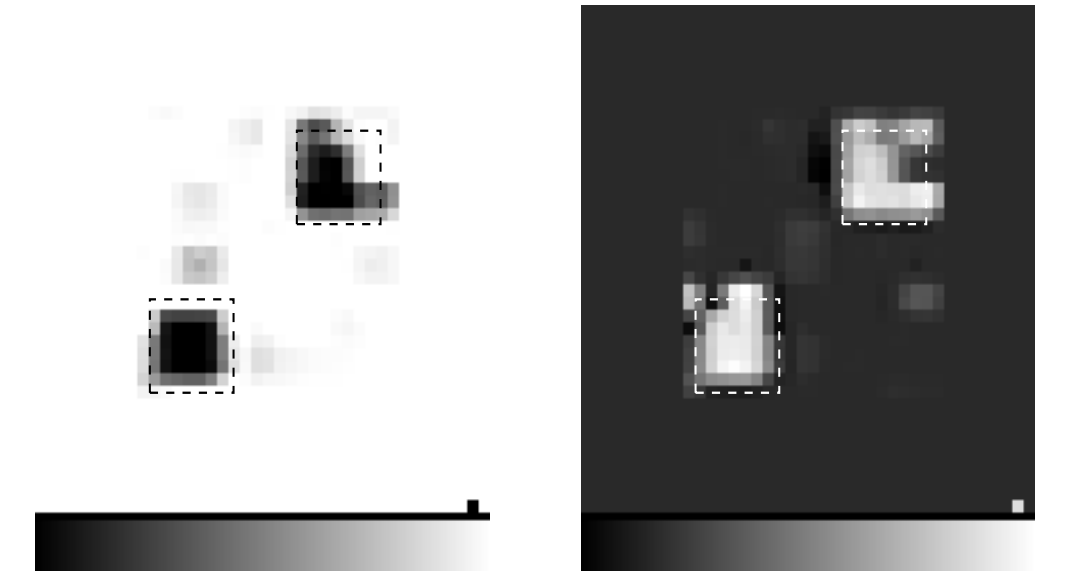

0.6 $Re\{\tau(x,y)\}$ 0.0 0.0 $Im\{\tau(x,y)\}$ -0.47

(d)

Fig. 5 (*II*) - S. Caorsi *et al.*, "Detection and Imaging ..."

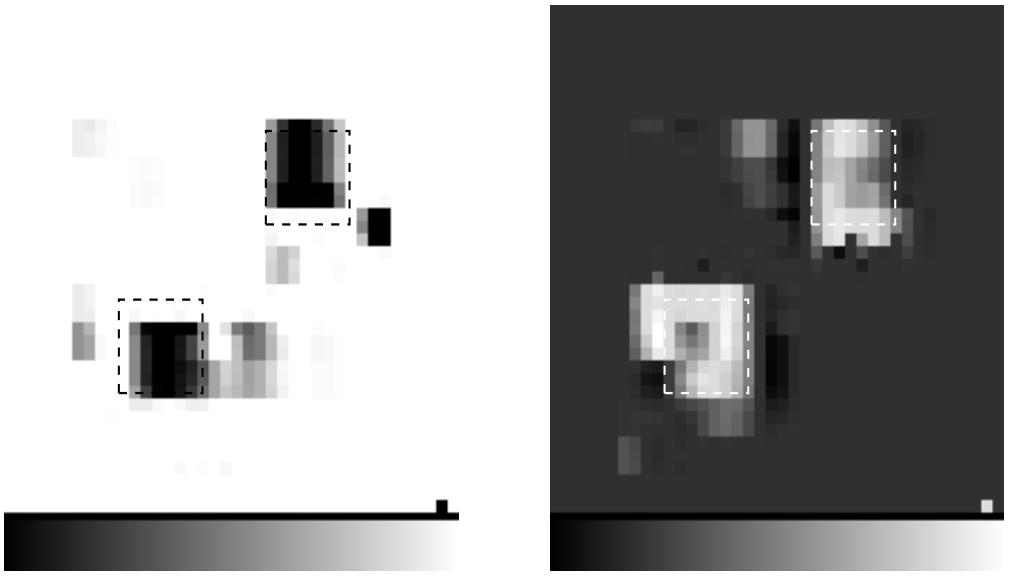

$0.6 \qquad Re\{\tau(x,y)\} \qquad 0.0 \quad 0.0 \qquad Im\{\tau(x,y)\} \qquad -0.47$

(e)

Fig. 5 (*III*) - S. Caorsi *et al.*, "Detection and Imaging ..."

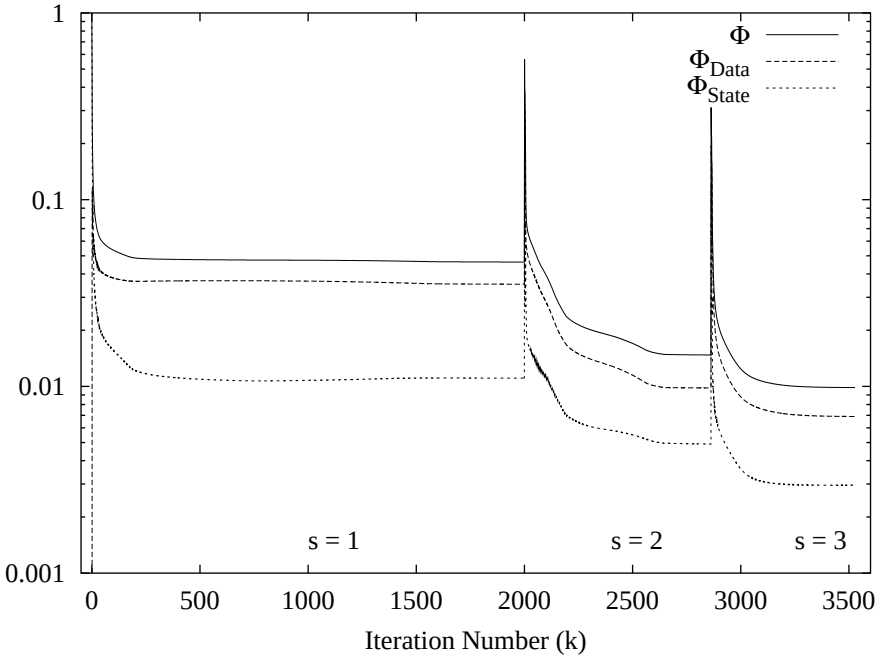

(a)

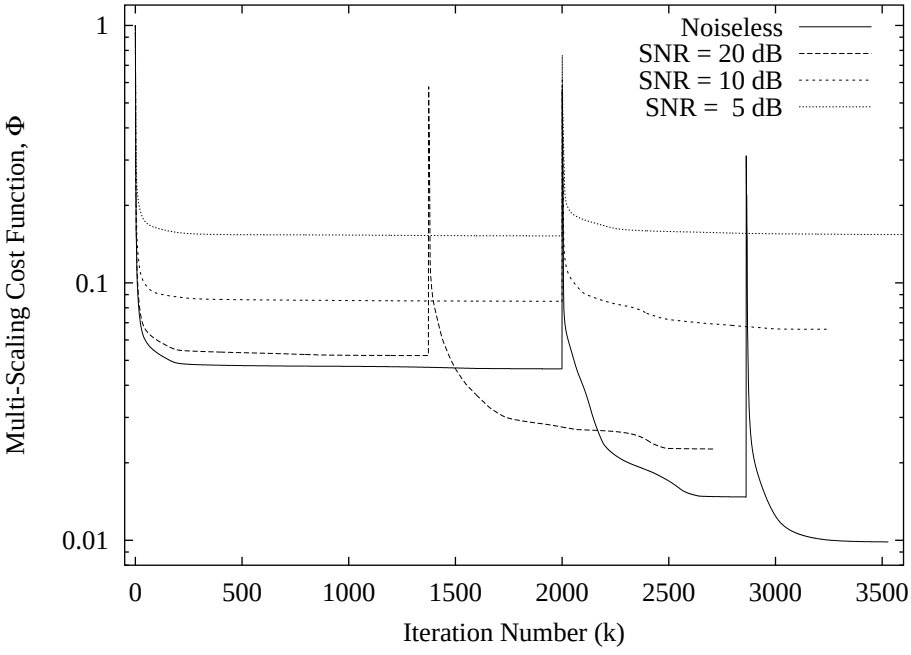

(b)

Fig. 6 - S. Caorsi *et al.*, "Detection and Imaging ..."

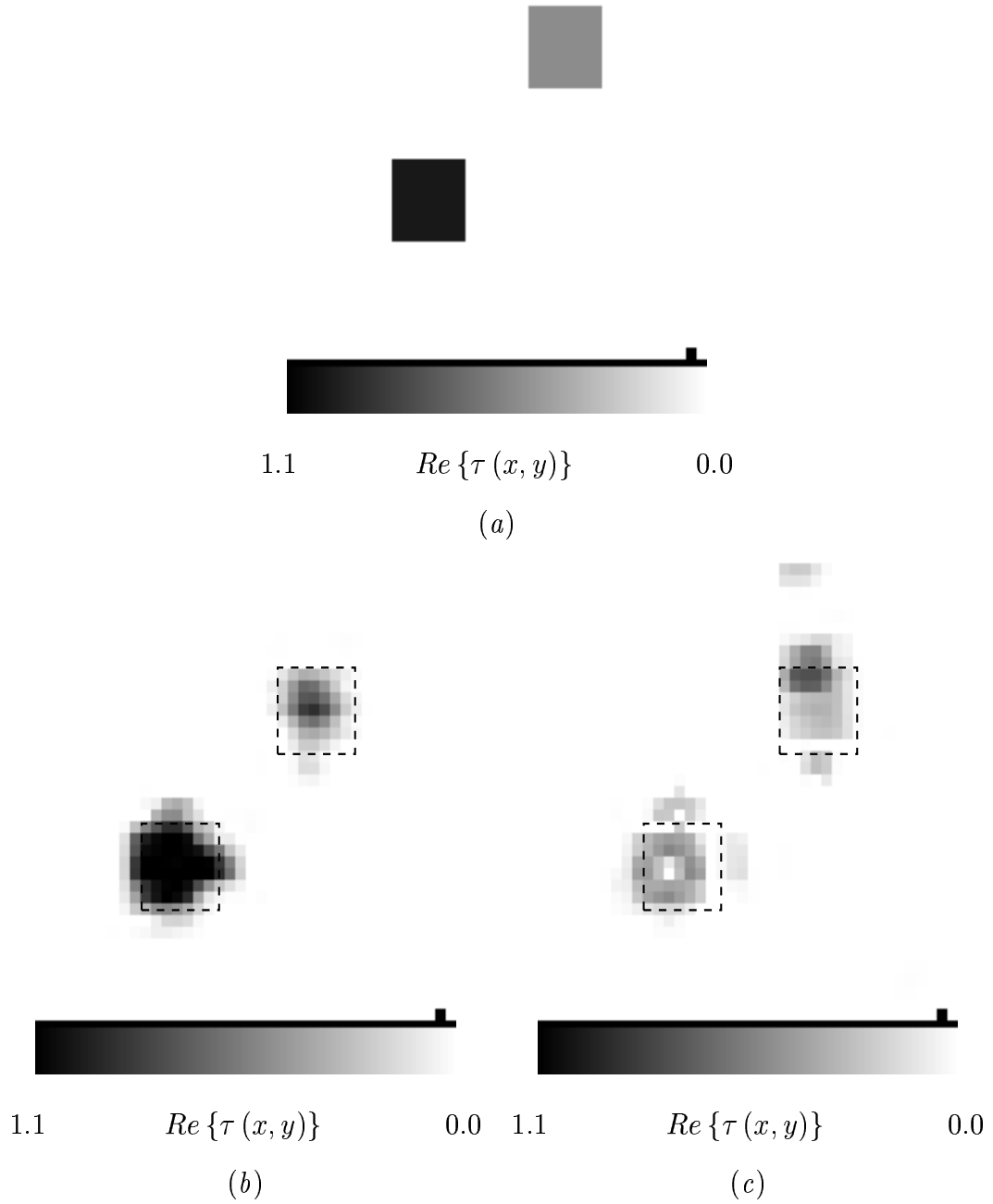

Fig. 7 - S. Caorsi *et al.*, "Detection and Imaging ..."

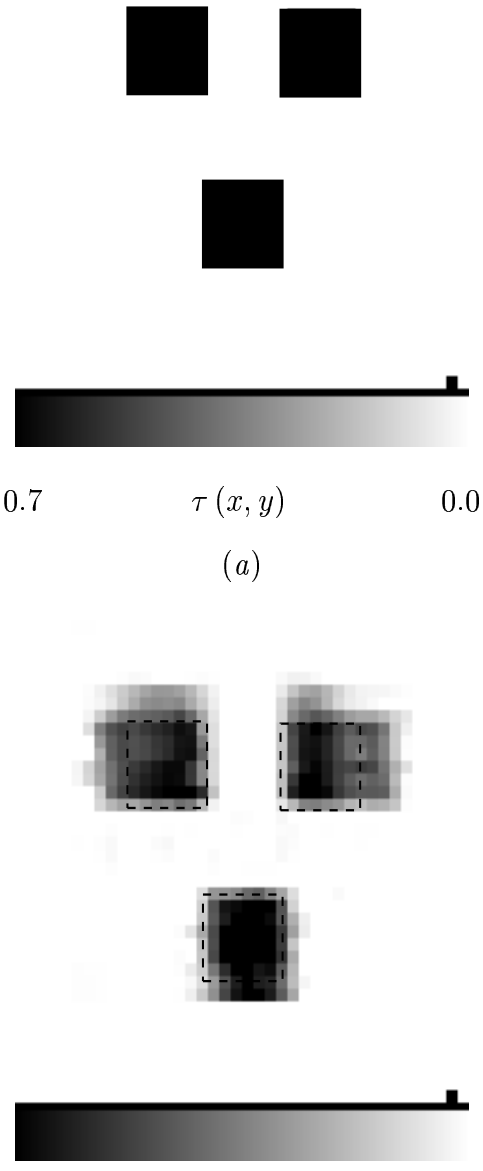

Fig. 8 - S. Caorsi *et al.*, "Detection and Imaging ..."

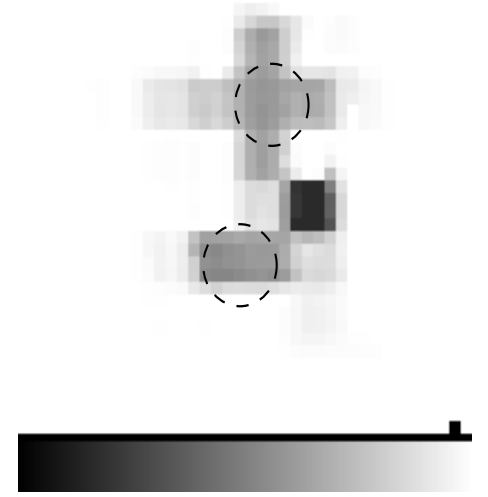

2.2 $\tau\,(x, y)$ 0.0

(a)

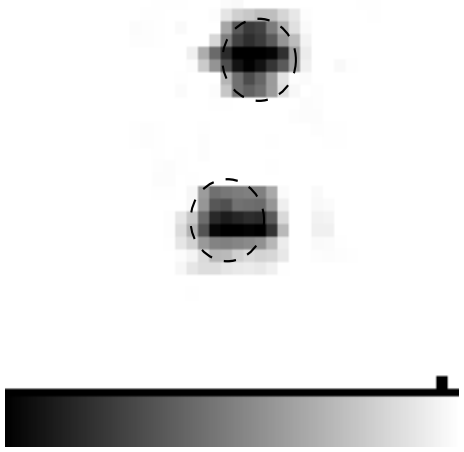

2.2 $\tau\,(x, y)$ 0.0

(b)

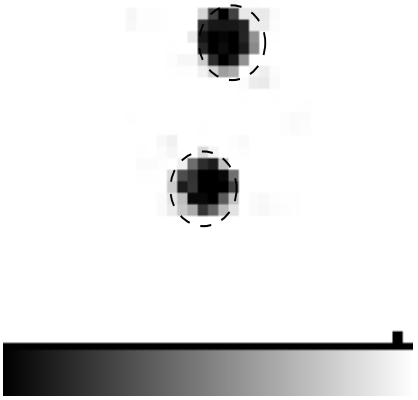

2.2 $\tau\,(x, y)$ 0.0

(c)

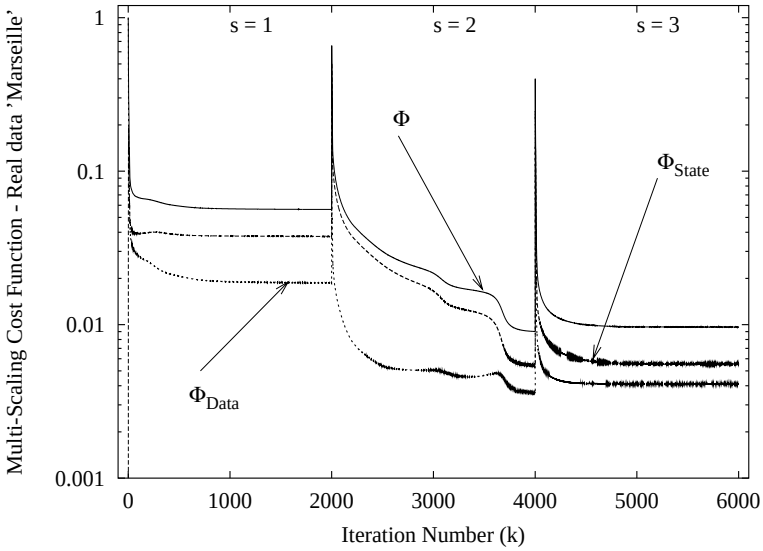

(d)

Fig. 9 - S. Caorsi *et al.*, "Detection and Imaging ..."

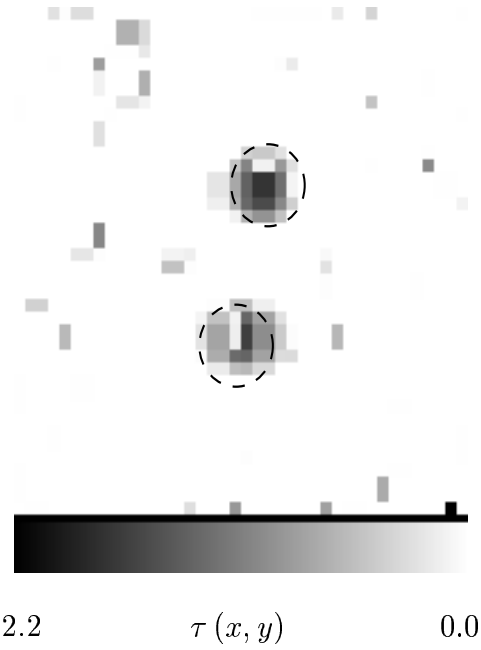

Fig. 10 - S. Caorsi *et al.*, "Detection and Imaging ..."

$Step\ No.$	1	2
ξ_{tot}	6.4	2.05
$\xi_{int}^{(1)}$	14.6	9.69
$\xi_{int}^{(2)}$	15.0	7.73
ξ_{ext}	6.25	2.02
$\rho^{(1)}$	0.037	0.031
$\rho^{(2)}$	0.054	0.034
$\Delta^{(1)}$	25.12	12.78
$\Delta^{(2)}$	22.12	11.08

Tab. I - S. Caorsi *et al.*, "Detection and Imaging ..."

$SNR \quad [dB]$	∞	20	10	5
ξ_{tot}	2.05	3.28	3.61	4.34
$\xi_{int}^{(1)}$	8.56	8.84	9.69	9.90
$\xi_{int}^{(2)}$	7.73	9.52	10.31	16.11
ξ_{ext}	2.02	2.61	3.25	3.81
$\rho^{(1)}$	0.031	0.072	0.083	0.21
$\rho^{(2)}$	0.034	0.068	0.098	0.26
$\Delta^{(1)}$	12.78	16.20	24.87	25.12
$\Delta^{(2)}$	11.08	17.11	21.94	29.88

Tab. II - S. Caorsi *et al.*, "Detection and Imaging ..."

	$Re\{\tau\}$				$Im\{\tau\}$	
$SNR\ [dB]$	ξ_{tot}	$\xi_{int}^{(1)}$	$\xi_{int}^{(2)}$	ξ_{ext}	$\xi_{int}^{(1)}$	$\xi_{int}^{(2)}$
∞	0.75	13.30	7.11	0.13	21.30	9.76
20	1.43	13.74	16.64	0.25	22.75	18.85
10	2.04	14.46	19.56	0.41	28.50	29.10
5	3.39	33.34	33.30	2.61	30.50	41.50

(a)

Tab. III(1) - S. Caorsi *et al.*, "Detection and Imaging ..."

$SNR \quad [dB]$	∞	20	10	5
$\rho^{(1)}$	0.037	0.036	0.084	0.22
$\rho^{(2)}$	0.033	0.038	0.063	0.10
$\Delta^{(1)}$	21.55	30.62	35.29	57.17
$\Delta^{(2)}$	23.41	26.01	32.14	78.18

(*b*)

Tab. III(2) - S. Caorsi *et al.*, "Detection and Imaging ..."

	IMM	$ISSM$
ξ_{tot}	1.89	2.76
$\xi_{int}^{(1)}$	17.09	21.60
$\xi_{int}^{(2)}$	13.29	24.12
ξ_{ext}	1.03	1.83
$\rho^{(1)}$	0.050	0.238
$\rho^{(2)}$	0.048	0.130
$\Delta^{(1)}$	6.22	25.06
$\Delta^{(2)}$	7.41	22.78

Tab. IV - S. Caorsi *et al.*, "Detection and Imaging ..."